Surface Engineering of Semiconducting Polymer Nanoparticles for Amplified Photoacoustic Imaging

Xu Zhen,[†] Xiaohua Feng,[‡] Chen Xie,[†] Yuanjin Zheng[‡] and Kanyi Pu[†,*]

[†]School of Chemical and Biomedical Engineering, Nanyang Technological University, 70
Nanyang Drive, Singapore, 637457

[‡]School of Electrical and Electronic Engineering, Nanyang Technological University, 50
Nanyang Avenue, Singapore, 639798

[*]Address correspondence to: kypu@ntu.edu.sg

ABSTRACT Despite the deeper tissue penetration of photoacoustic (PA) imaging, its sensitivity is generally lower than optical imaging. This fact partially restricts the applications of PA imaging and greatly stimulates the development of sensitive PA imaging agents. We herein report that the surface coating of semiconducting polymer nanoparticles (SPNs) with the silica layer can simultaneously amplify fluorescence and PA brightness while maintaining their photothermal conversion efficiency nearly unchanged. As compared with the bare SPNs, the silica-coated SPNs (SPNs-SiO_2) have higher photothermal heating rate in the initial stage of laser irradiation due to the higher interfacial thermal conductance between the silica layer and water relative to that between the SP and water. Such an interfacial effect consequently results in sharp temperature increase and in turn amplified PA brightness for SPNs-SiO_2. By conjugating polyethylene glycol (PEG) and cyclic-RGD onto SPNs-SiO_2, targeted PA imaging of tumor in living mice is demonstrated after systemic administration, showing a high signal to background ratio. Our study provides a surface engineering approach to amplify the PA signals of organic nanoparticles for molecular imaging.

KEYWORDS: Semiconducting polymer nanoparticles, Photoacoustic imaging, Surface engineering, Tumor imaging

1. Introduction

Photoacoustic (PA) imaging as a hybrid non-ionizing imaging modality that measures the conversion of photon energy into acoustic pressure waves, which provides deep tissue penetration as compared with optical imaging due to the minimized scattering of acoustic waves relative to light [1, 2]. PA imaging has been not only used to understand fundamental biology such as imaging of diseases biomarkers [3, 4], brain function [5] and angiogenesis [6], but also involved in preclinical and clinical studies such as cancer diagnostics [7, 8], guided sentinel lymph node biopsy [9], brain imaging [10] and dosimetry in thermal therapy [11]. However, as PA signals are mainly determined by the absorption and photothermal conversion of imaging agents, the sensitivity of PA imaging is generally lower than optical imaging [12]. To advance the applications of PA imaging in life science, imaging agents with high PA brightness are highly desired, which can also minimize the dosage required for *in vivo* studies and in turn alleviate the potential issue of toxicity.

Semiconducting polymer nanoparticles (SPNs) have recently been used for PA imaging in addition to small-molecule organic dyes [13, 14], fluorescent proteins [15, 16], gold nanoparticles [17], carbon nanotubes [18-21], two-dimensional materials [22-24], up-conversion nanoparticles [25] and porphysomes [26-28]. SPNs are made from semiconducting polymers (SP) with π-electron delocalized backbones, which have proved as versatile photonic nanomaterials for a variety of molecular imaging and theranostic applications [29-39]. In particular, SPNs have been developed into smart activatable probes for *in vivo* PA imaging of tumor [40], reactive oxygen species [41] and pH [42]. SPNs often have higher photostability and PA brightness as compared with other PA agents such as carbon nanotubes and gold nanorods [41, 43]. These intrinsic merits in conjunction with their organic and biologically benign ingredients place SPNs at the forefront of PA imaging.

To improve the sensitivity of SPNs for PA imaging, we not only investigated the relationship between the structure and PA properties of SPs [44] but also proposed an intraparticle engineering approach [45]. As compared with massive screening of SPs, the intraparticle doping approach is a more facile way that avoids time-consuming synthesis. The doping approach incorporates a secondary component into SPNs that serves as the electron acceptor to create photoinduced electron transfer (PET) (**Figure 1a**), that promotes nonradiative decay, quenches the fluorescence and converts this part of photon energy into extra heat, ultimately augmenting PA signals. In addition, enhanced heat generation increases maximum photothermal temperature and thus benefits photothermal therapy [45]. However, this approach can only be applied to fluorescent SPNs, and after doping, SPNs are no longer light-emitting, which comprises the capability for complementary fluorescence imaging. Moreover, some other materials such as single-layer MoS_2 nanosheets [46] and reduced graphene oxide coated gold nanorods [47] have been used to amplify PA signals for sensitive PA imaging.

In this study, we report a general surface engineering approach to develop multilayered SPNs with simultaneously amplified fluorescence and PA brightness for *in vivo* imaging. The multilayered SPNs contains a hydrophobic SP core coated with an optically inner silica shell (**Figure 1a**). Note that although silica-coated nanoparticles composed of small-molecule dyes have been reported [48], the effect of silica on the PA properties has yet to be revealed. We synthesized silica-coated SPNs (SPNs-SiO_2) and compared their optical, photothermal and PA properties with the uncoated SPNs. To demonstrate the generality of this approach, both nonfluorescent (SP1) and fluorescent (SP2) polymers were tested. We found that SPNs-SiO_2 had higher PA brightness than the uncoated SPNs. We thus carried out the finite element analysis (FEA) simulation to reveal the underlying mechanism involved. The results revealed that the photothermal heating rate of SPN-

SiO_2 is faster than that of the uncoated SPNs due to the higher heat interfacial conductance for the interface between the silica layer and water as compared with that between the SP core and water. Such an interfacial effect eventually led to the higher PA signals for SPN-SiO_2 relative to that for the uncoated SPNs. To demonstrate the proof-of-concept imaging application, SPNs-SiO_2 were conjugated with peptide and applied for PA imaging of tumor in living mice.

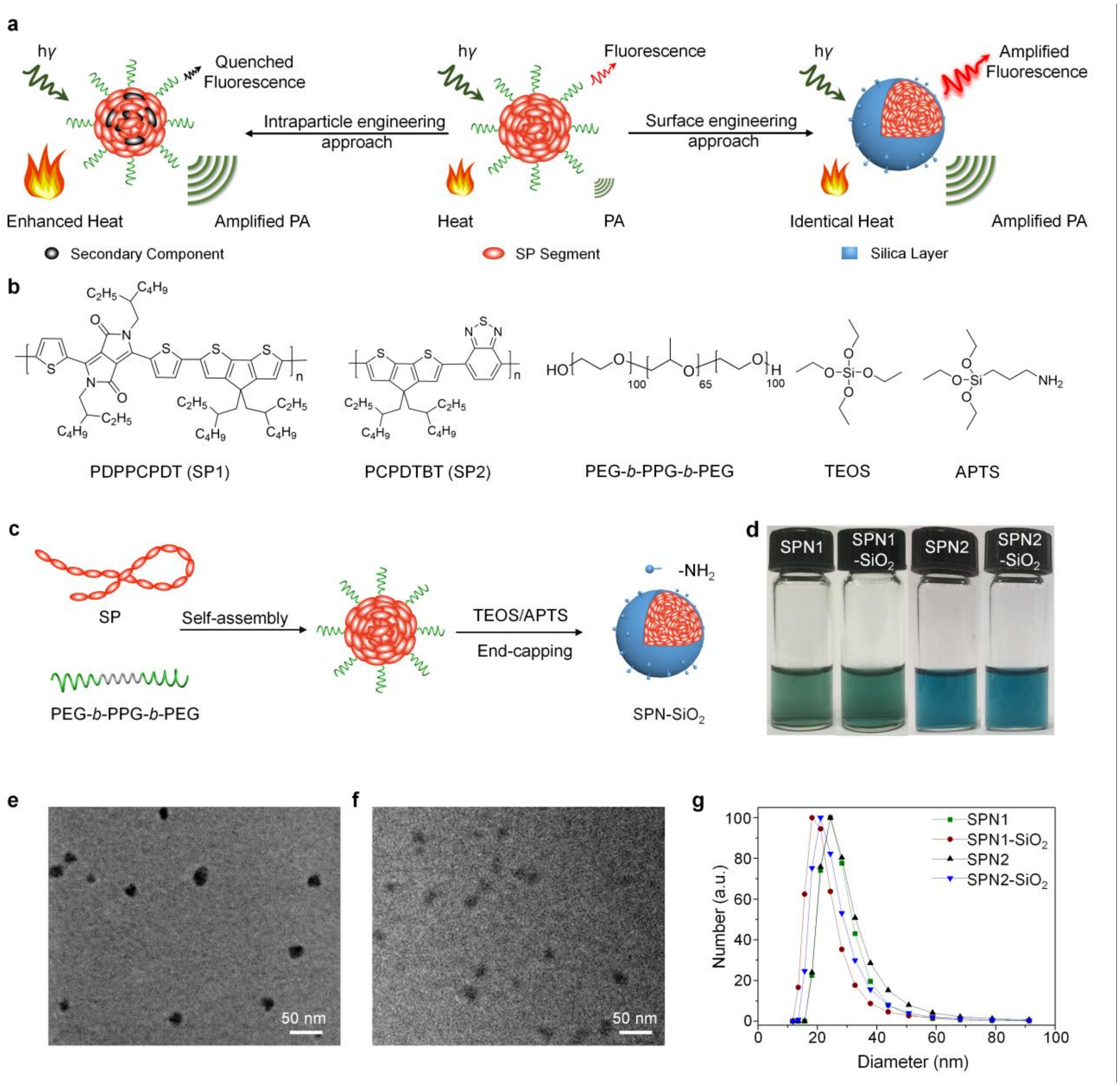

Figure 1. Synthesis and characterization of SPNs. (**a**) Schematic illustration of intraparticle engineering and surface engineering approaches for amplified PA imaging. (**b**) Chemical

structures of reagents used for preparation of SPNs, including PDPPCPDT, PCPDTBT, PEG-*b*-PPG-*b*-PEG, TEOS, and APTS. (**c**) Schematic illustration of the preparation of SPN-SiO_2. (**d**) Photography of the solutions of SPNs. [SPN] = 20 μg mL^{-1}. Representative TEM images of SPN1 (**e**) and SPN1-SiO_2 (**f**). (**g**) Representative DLS profiles of SPNs in PBS.

2. Results and discussion

Two near-infrared (NIR) absorbing SP analogues, poly(cyclopentadithiophene-*alt*-diketopyrrolopyrrole) (PDPPCPDT, SP1) and poly(cyclopentadithiophene-*alt*-benzothiadiazole) (PCPDTBT, SP2), were used to synthesize the SPNs (**Figure 1b**). Different from its analogue SP2, SP1 had the structure unit of diketopyrrolopyrrole in the backbone, which narrowed down the band gap and red-shifted the absorption. The uncoated SPNs (SPN1 and SPN2) were synthesized from nanoprecipitation with the amphiphilic triblock copolymer Polyethylene glycol-*b*- Polypropylene glycol-*b*-Polyethylene glycol (PEG-*b*-PPG-*b*-PEG). To prepare the silica-coated SPNs (SPN1-SiO_2 and SPN2-SiO_2), a THF mixture of SPs and PEG-*b*-PPG-*b*-PEG at the weight ratio of 1:100 was first prepared and evaporated to yield a solid thin film. After reconstituting in the HCl solution under ultrasonication, the silicate condensation of tetraethyl orthosilicate (TEOS) efficiently was conducted to form a thin silica shell on the surface of SPNs-SiO_2. At last, (3-aminopropyl)triethoxysilane (APTS) was added to the reaction solution to terminate the silicate condensation and also to generate the amine groups on the nanoparticle surface for post-bioconjugation (**Figure 1c**). The resulted solutions of SPNs-SiO_2 were translucent (**Figure 1d**).

Transmission electron microscopy (TEM) showed that both SPNs and SPNs-SiO_2 had uniform spherical morphology with the average diameter of ~ 20 and 15 nm for SPN1 and SPN-SiO_2 (**Figures 1e&1f**), respectively. Dynamic light scattering (DLS) further confirmed that the average hydrodynamic diameters of SPNs-SiO_2 were smaller than that of SPNs (**Figure 1g**), which were 24, 18, 24 and 21 nm for SPN1, SPN1-SiO_2, SPN2 and SPN2-SiO_2, respectively. This is caused by the fact that after the silicate condensation, SPNs-SiO2 were condensed and became more compact relative to bare SPNs. The hydrodynamic diameters were slightly larger than the diameters measured by TEM, probably because the sample preparation of TEM caused the shrinkage of nanoparticles. The nanoparticles remained stable for months with no obvious size change (**Figure S1**, Supporting Information), demonstrating the long-term aqueous stability of these SPNs.

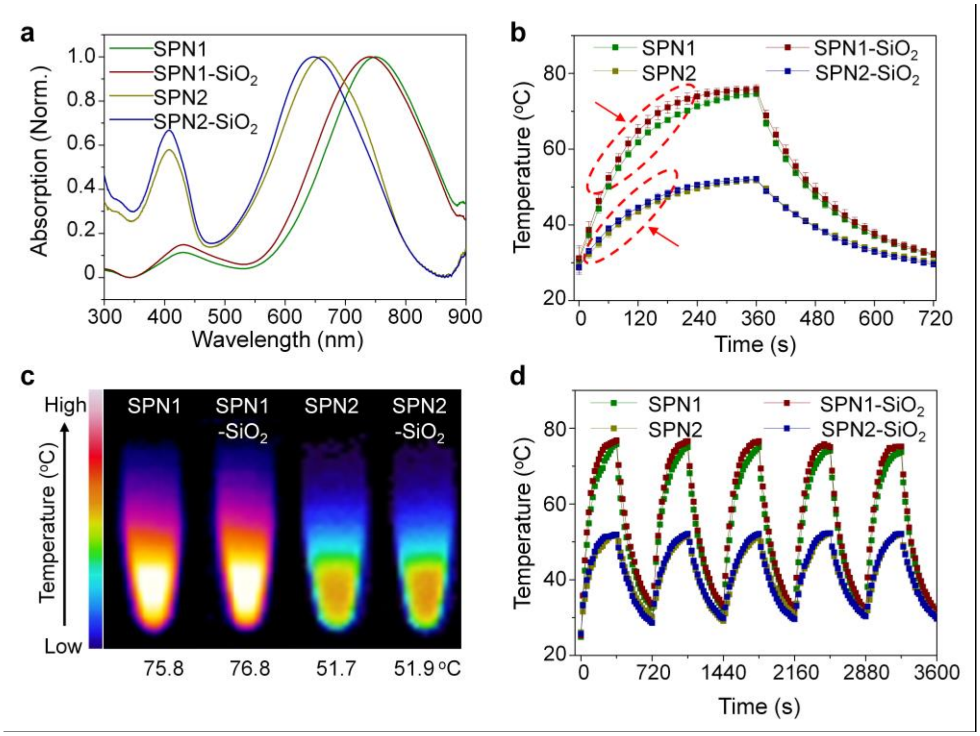

Figure 2. Absorption and photothermal characterization of SPNs. (**a**) Absorption spectra of SPNs: SPN1, SPN1-SiO_2, SPN2 and SPN2-SiO_2. (**b**) Temperatures of SPN solutions as a function of laser irradiating time. The different temperature increase rates between SPNs and SPNs-SiO_2 are indicated with the red dashed circles pointed with the red arrows. (**c**) Thermal images of SPNs solutions at their respective maximum photothermal temperatures. (**d**) Stability study of SPNs under the photothermal heating and natural cooling cycles. [SPN] = 20 μg mL^{-1} in 1 × PBS (pH = 7.4). The laser irradiation wavelength was at 808 nm with a power of 1 W cm^{-2}.

The absorption and photothermal properties of SPNs were studied and compared in phosphate buffered saline (PBS) (pH = 7.4). For each pair of SPNs, the absorption spectra curves of SPNs and SPNs-SiO_2 were similar (**Figure 2a**), consistent with the fact that absorption of SPNs was mainly determined by the molecular structures of SPs inside the SPN core. Owing to the enhanced charge transfer, the absorption maxima of SPN1 (750 nm and (740 nm) SPN1-SiO_2) were red-shifted by ~90 relative to those of SPN2 (660 nm and (650 nm) SPN2-SiO_2). The peak mass extinction coefficients of SPN1 and SPN1-SiO_2 were 87 $cm^{-1}mg^{-1}$ mL, similar to those of SPN2 and SPN2-SiO_2 (90 cm^{-1} mg^{-1} mL).

Under continuous laser irradiation at 808 nm, all the SPNs showed gradually increased solution temperatures and all the nanoparticles reached plateau before t = 360 s (**Figure 2b**). The superficial silica layer of SPNs-SiO_2 did not affect the maximum photothermal temperature of SPNs (**Figure 2c**): the maximum photothermal temperatures of each pair of SPNs were nearly the same (75.8 *vs* 76.8 ^{o}C for SPN1 and SPN1-SiO_2, and 51.7 *vs* 51.9 ^{o}C for SPN2 and SPN2-SiO_2, respectively). The photothermal conversion efficiencies of SPN1, SPN1-SiO_2, SPN2, and SPN2-SiO_2 at 808 nm were calculated to be 19.7, 18.9, 27.5, and 28.1%, respectively. The photothermal stability was studied by reversibly heating and cooling the nanoparticle solutions (**Figure 2d**). The maximum temperatures of SPNs remained nearly the same for at least 5 cycles, demonstrating that all the SPNs had good photothermal stability.

The maximum photothermal temperatures and conversion efficiencies of SPNs were mainly determined by the molecular structures of SPs used for preparation of SPNs but not affected by the surface structures. However, the temperature of SPN1-SiO_2 was higher than that of SPN1 at each time point before t = 240 s (**Figure 2b**), meaning that the photothermal heating rate of SPN1-SiO_2 was larger than that of SPN1 in the initial stage of laser irradiation. Thus, SPN1-SiO_2 required only 240 s to reach the maximum photothermal temperature, which took additional 120 s for SPN1 (360 s in total) to reach the maximum temperature (**Figure 2b**). Similar trend was observed for SP2-based nanoparticles. These results demonstrated that the silica layer affected the photothermal heating rate for SPNs-SiO_2. As silica was optically inert, it should only be able to facilitate the heat diffusion from the optically active SP core to the surrounding water environment. Thus, the increased heating rates for the silica coated SPNs *vs* the uncoated SPNs indicated that the interface silica to water had a lower interfacial resistance as compared with that of the SP core to water. This phenomenon was also observed for silica-coated gold nanoparticles [49-51].

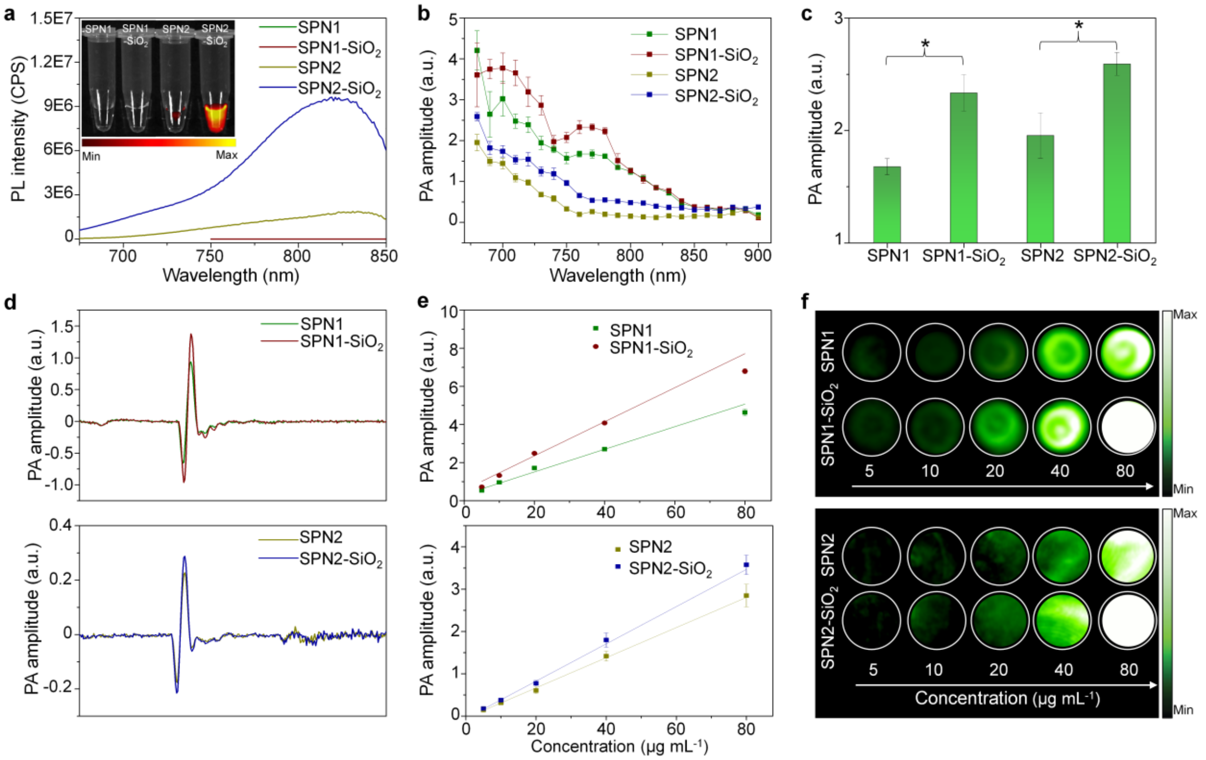

Figure 3. Fluorescence and photoacoustic properties of SPNs. (**a**) Fluorescence spectra of SPNs in 1 × PBS (pH = 7.4). Inset: Representative IVIS fluorescence images of SPNs in 1 × PBS (pH = 7.4). [SPN] = 2 μg mL^{-1}. (**b**) PA spectra of SPNs in 1 × PBS (pH = 7.4). (**c**) Comparison of PA amplitudes of SPN1 and SPN1-SiO_2 at 760 nm, and SPN2 and SPN2-SiO_2 at 680 nm under the same concentration, respectively. [SPN] = 20 μg mL^{-1} ($*p < 0.01$, $n = 5$). (**d**) PA signals of SPN1

and SPN1-SiO_2 at 760 nm (top) and SPN2 and SPN2-SiO_2 at 680 nm (down) in the same optical concentration. (**e**) The PA amplitudes at 760 nm as a function of concentrations of SPN1 and SPN1-SiO_2 (top) and at 680 nm as a function of concentrations of SPN2 and SPN2-SiO_2 (down). (**f**) The PA images of SPN1 and SPN1-SiO_2 (top) and SPN2 and SPN2-SiO_2 (down) at different concentrations.

The fluorescence and PA properties of SPNs were studied and compared in PBS at pH = 7.4. SPN1 and SPN1-SiO_2 were nearly non-fluorescent, while SPN2 and SPN2-SiO_2 showed the emission maximum at 835 and 820 nm, respectively (**Figure 3a & Figure S2**, Supporting Information). With the silica coating, SPN2-SiO_2 had the fluorescence quantum yield (1.46 %) that was 5.22-times higher than SPN2 (0.28 %) (**Figure 3a**). This is consistent with our and others previous studies that silica coating often increases the fluorescence of organic dye-doped nanoparticles, because it can effectively reduce the interaction between the fluorescent component and water molecules and provides a relatively hydrophobic environment [52, 53].

The PA spectra of SPNs were acquired at the same mass concentration of SPs by pulsed laser irradiation ranging from 680 to 950 nm (**Figure 3b**). Similar PA spectra profiles with the peak at 760 and 680 nm were observed for SP1- and SP2-based SPNs, respectively. This was consistent with their absorption spectra, showing that silica coating did not change the PA spectral file for SPNs. However, the PA amplitudes of the silica-coated SPNs were ~1.4 higher than the corresponding uncoated SPNs (**Figure 3c&3d**). Such a silica coating amplified PA signals were observed regardless of the nanoparticles concentrations (**Figure 3e**). Different from our previous intraparticle PET approach wherein the PA signals were enhanced along with the decreased fluorescence (Figure 1a), the surface coating of SPNs with a silica layer not only enhanced the fluorescence but also amplified the PA brightness of SPNs.

The PA signal depends on the following factors: i) the account of incident photons be absorbed and converted to heat, and ii) the rate of the generated heat diffusing out from the nanoparticles during thermoelastic expansion and wave generation [51]. In this study, the maximum photothermal temperatures of SPN and SPN-SiO_2 were almost the same (Figure 2c), demonstrating that the same amounts of photons can be absorbed and converted into heat (Factor i). Thus, this implies that the rate of the generated heat diffusing out from the SP core (Factor ii) plays an important role in determining the PA signals of SPNs and SPNs-SiO_2. By virtue of the silica layer in the surface, the heat diffusion from the SP core of SPNs-SiO_2 to the surrounding fluid is faster than that for SPNs. This was witnessed by the fact that the temperature of SPNs-SiO_2 increased faster than that of SPNs at the beginning of continuous laser irradiation at 808 nm (**Figure 2b**).

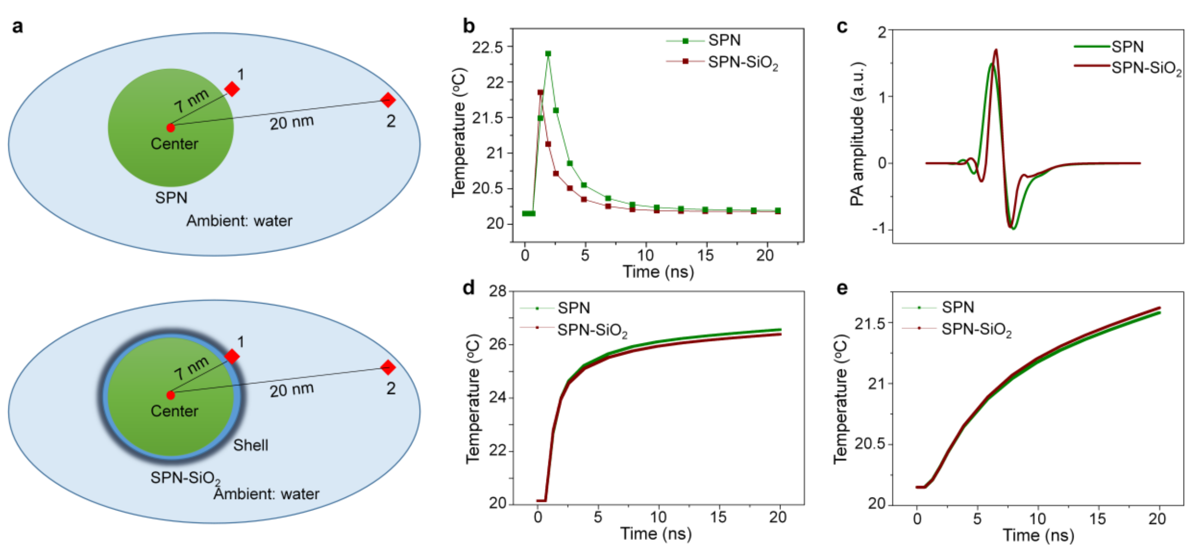

Figure 4. Simulation of photothermal and PA properties of SPNs. (**a**) Schematic illustration of the COMSOL simulation for nanoparticles**.** (1 and 2 are the two test points for measuring temperature and photoacoustic signal) (**b**) Simulation of the temperature near the surface of the SPNs (Point 1) after a temporal laser pulse. (**c**) Simulation of PA signals near the surface of SPNs (Point 1) after a temporal laser pulse. (**d**) Simulation of the temperature 7 nm away from the center

of SPN (Point 1) after a continuous laser pulse. (**e**) Simulation of the temperature 20 nm away from the center of SPN (Point 2) after a continuous laser pulse.

To investigate the detailed mechanism that governs the different photothermal and PA properties of silica-coated and uncoated SPNs, a finite element analysis (FEA) simulation was conducted in COMSOL multiphysics (COMSOL Inc, USA). In the simulation, the cores of both nanoparticles ($SPN-SiO_2$ and SPN) were set to have a semidiameter of 6 nm (**Figure 4**). According to the literature [54], the PEG-*b*-PPG-*b*-PEG templated coating of nanoparticles usually resulted in a thin silica shell, and thus the silica coating layer of $SPN-SiO_2$ was set to have the thickness of 1 nm (**Figure 4a**). The surrounding fluid environment was set to be water. For PA simulations, the laser heating pulse was set to 1 ns; whereas for photothermal simulations, the laser heating was set to be continuous. The temperatures of water at the distance that is 7 nm away from the centre of SPN and $SPN-SiO_2$ (Point 1) were compared after 1 ns laser heating (**Figure 4**). $SPN-SiO_2$ showed sharper increase but lower peak temperature than that of SPN (**Figure 4b**). This was due to the fact that the interface between the silica layer and water had the higher heat interfacial conductance relative to that of the SP core and water, which was consistent with the experimental photothermal results (**Figure 2b**). The reduced interfacial resistance accelerated the heat dissipation from $SPN-SiO_2$ to the surrounding water, leading to the sharper temperature increase as compared to that for SPN as well as a lower peak temperature at the interface of $SPN-SiO_2$ based on the formula of $\Delta T = RQ$ (where Q is the heat flux through the interface and R is the interfacial resistance) [55, 56]. The PA simulation were performed in two steps: in the first step, the heat transfer simulation was conducted using the heat transfer module in COMSOL; in the second step, the heat transfer simulation results were coupled to the acoustic module to obtain the final PA signals. The separation into two steps could be justified by the wave equation of PA:

$$\nabla^2 p(r,t) - \frac{1}{c^2}\frac{\partial^2}{\partial t^2} p(r,t) = -\frac{\Gamma}{c^2} A(r) \frac{\partial}{\partial t} H(t) \tag{1}$$

in which $p(r,t)$ and c represent the PA pressure and speed of sound, respectively. Γ signifies the Grueneisen parameter of water. $A(r)$ and $H(t)$ denote the heating function's spatial distribution and temporal characteristics, respectively. The wave equation could be solved by using the Green's function method as:

$$p(r,t) = \frac{\Gamma}{c^2}\frac{\partial}{\partial t} H(t) \iiint \frac{d^3 r'}{|r - r'|} A(r') \Bigg|_{|r-r'|=ct} \tag{2}$$

r and r' denote the position where the PA waves are to be detected and the position inside the material, respectively [57]. From the analytic solution, it is observed that the PA signal could be obtained numerically once one have the solution for the heating function ($A(r)$ and $H(t)$). The analytic equation also indicates that the PA amplitude is proportional to the derivative of temperature (heating function). Thereby, the higher interfacial heat conductance of SPN-SiO_2 resulted in a sharper temperature increase, and consequently led to a larger PA signal. As a result of such a silica-induced interfacial effect, the PA signals generated by SPN-SiO_2 was calculated to be 1.2 times higher than that of SPN (**Figure 4c**), consistent with the experimental observation (**Figure 3c**).

The photothermal responses of SPN-SiO_2 and SPN under continuous laser heating at 7 (Point 1) and 20 nm (Point 2) away from the absorbing nanoparticle centre were compared, respectively (**Figures 4d&4e**). As compared with SPN, SPN-SiO_2 with the higher interfacial heat conductance indeed displayed slightly lower temperature at point 1 under continuous laser heating (**Figure 4d**); however, SPN-SiO_2 displayed slightly higher temperature at point 2 than that of SPN under continuous laser heating (**Figure 4e**). This should be attributed to the fact that the same heat were generated from SPN-SiO_2 and SPN. With more heat transferred into the far field (Point 2), relatively less heat left at the near field (Point 1) for SPN-SiO_2 relative to that of SPN. The experimental observation and simulation results demonstrated that the higher heat interfacial conductance for the interface between the silica layer and water relative to that of the SP core and water is the origin of increased photothermal heating rate and amplified PA brightness for SPN-SiO_2 as compared to SPN.

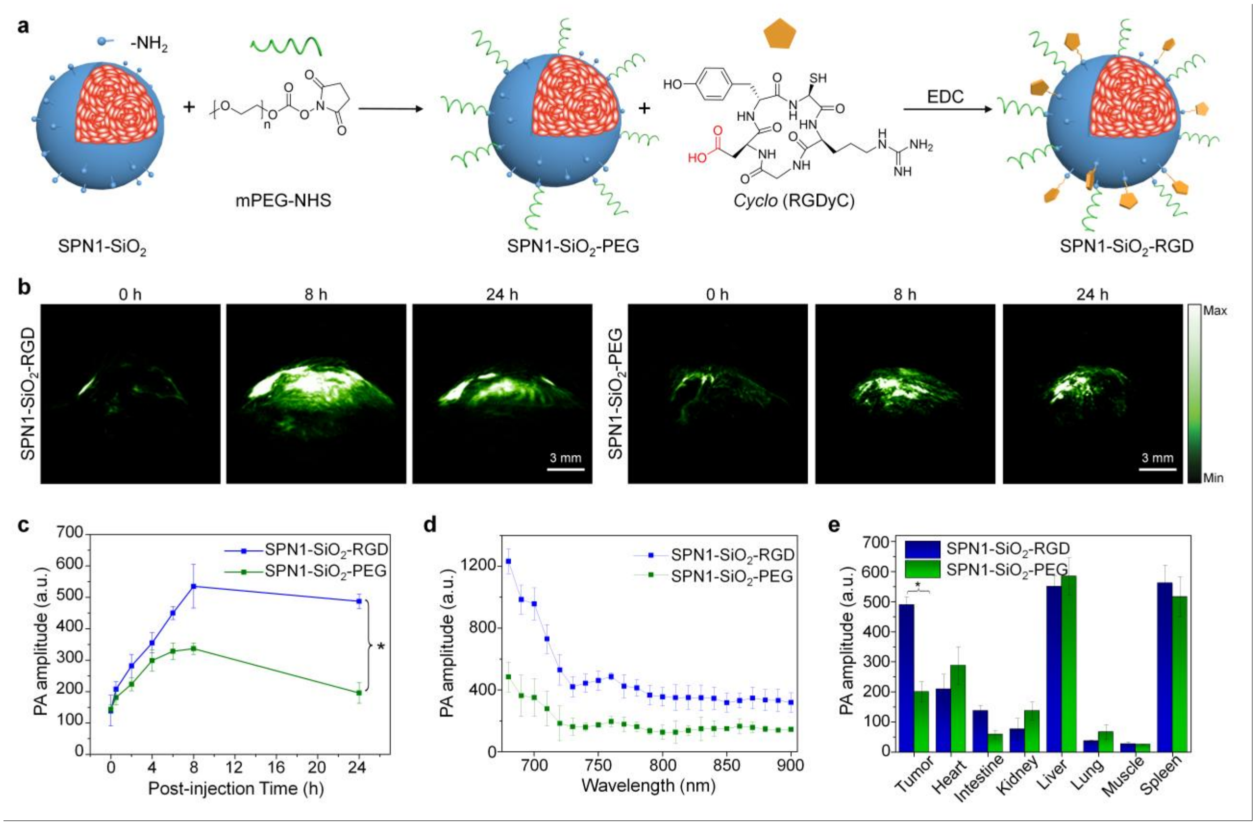

Figure 5. *In vivo* PA imaging of xenograft 4T1 tumors in living mice. (a) Synthesis of SPN1-SiO_2-PEG and SPN1-SiO_2-RGD. (**b**) Representative PA images of subcutaneous tumor after intravenous administration of SPN1-SiO_2-RGD or SPN1-SiO_2-PEG (150 µg/mL, 0.2 mL) through tail vein injection for 0, 8 and 24 h, respectively. The representative PA maximum imaging projection (MIP) images with axial view for the tumors of SPN1-SiO_2-RGD or SPN1-SiO_2-PEG-injected mice. (**c**) Quantification of PA intensities at 760 nm of tumor as a function of post-injection time of SPN1-SiO_2-RGD or SPN1-SiO_2-PEG.*$P < 0.05$, in comparison between PA

intensities at 760 nm of tumor of 2, 4, 6, 8, and 24 h of SPN1-SiO_2-RGD and SPN1-SiO_2-PEG. (**d**) *In vivo* real-time PA spectra extracted from the tumor areas of living mice after intravenous administration of SPN1-SiO_2-RGD or SPN1-SiO_2-PEG for 24 h. (**e**) *Ex vivo* PA quantification at 760 nm of major organs of mice 24 h after intravenous administration of SPN1-SiO_2-RGD or SPN1-SiO_2-PEG (*$p < 0.01$, $n = 3$).

SPN1-SiO_2 was developed into targeted probes for *in vivo* PA imaging of tumor in living mice, as it has the longest PA maximum and highest PA brightness among all SPNs. To reduce the reticuloendothelial system (RES) uptake and prolong the circulation time *in vivo*, SPN1-SiO_2 were conjugated with NHS-PEG *via* nucleophilic substitution reaction between the amine group of SPN1-SiO_2 and NHS group (**Figure 5a**), leading to SPN1-SiO_2-PEG. To afford the targeting capability, SPN1-SiO_2-PEG were further conjugated with a cyclic-RGD *via* a *N*-(3-dimethylaminopropyl)-*N*'-ethylcarbodiimide hydrochloride (EDC) coupling reaction between the amino group on the nanoparticle surface and the carboxyl group of cyclic-RGD, affording SPN1-SiO_2-RGD. No obvious difference in size (21.3 ± 1.2 and 20.2 ± 0.8 nm for SPN1-SiO_2-RGD and SPN1-SiO_2-PEG, respectively) was observed as compared with SPN1-SiO_2 (18.8 ± 2.2 nm) (**Figure S3**, Supporting Information). In addition, no obvious cytotoxicity was detected for both SPN1-SiO_2-RGD and SPN1-SiO_2-PEG against human breast cancer 4T1 cells (**Figure S4**, Supporting Information), confirming the suitability of SPN1-SiO_2-RGD and SPN1-SiO_2-PEG for biological applications.

The imaging capability of SPN1-SiO_2-RGD and SPN1-SiO_2-PEG were tested in the mouse model of subcutaneous 4T1 xenograft tumor. After systemic administration of SPN1-SiO_2-RGD or SPN1-SiO_2-PEG into the tumor-bearing living mice through tail vein, the PA images were longitudinally recorded and quantified (**Figure 5b**). The PA signals in tumor regions gradually increased for both nanoparticles over time and reached maximum at 8 h post-injection for both

SPNs (Figure 5c). In particular, SPN1-SiO_2-RGD injected mice had much higher PA intensities in tumor region as compared to those for SPN1-SiO_2-PEG at each post-injection time point. This was attributed to the presence of cyclic-RGD in SPN1-SiO_2-RGD, which targeted the $\alpha_v\beta_3$ integrin receptors overexpressed on the surface of 4T1 cells and subsequently promoted the tumor uptake of nanoparticles [58, 59]. At 8 h post-injection, the PA signals of tumors reached its maximum for both SPNs. At this time point, the intensity for SPN1-SiO_2-RGD injected mice was 1.60-fold higher than that for SPN1-SiO_2-PEG injected mice, and also 3.85 higher than that of the tumor background. Such a PA intensity difference could be obviously visualized in the PA images, and the enhanced PA signals permitted clear visualization of tumors using SPN1-SiO_2-RGD (**Figure 5b**).

To further confirm the source of enhanced PA signals in tumors, the real-time *in vivo* PA spectra were extracted from the tumors of SPN1-SiO_2-RGD or SPN1-SiO_2-PEG-injected mice. The *in vivo* spectra resembled that of SPN1-SiO_2 in solution (**Figure 5d** *vs* **Figure 3b**), validating that the enhancement of PA signal in tumor regions was originated from the nanoparticle accumulation. The *ex vivo* biodistribution of SPN1-SiO_2-RGD or SPN1-SiO_2-PEG injected mice were acquired at 24 h using PA quantification (**Figure 5e**). SPN1-SiO_2-RGD and SPN1-SiO_2-PEG have similar dynamic biodistributuion in major organs such as liver and spleen. However, the targeting capability of SPN1-SiO_2-RGD led to 2.45-fold higher particle accumulation in tumor as compared with SPN1-SiO_2-PEG, which was consistent with the real-time PA measurement (**Figures 5c&5d**). These data not only proved the utility of the silica-coated SPNs both actively and passively targeting probes for *in vivo* PA imaging of tumor.

3. Conclusions

In summary, we have designed and synthesized two classes of SPNs with different surface structures and compared their optical, photothermal and PA properties in details. With surface coating of SPNs with a silica layer, the fluorescence and PA brightness can be increased 5.2 and 1.4-fold, respectively; whereas, their photothermal conversion efficiency remains nearly the same. Such a surface-coating induced PA amplification is different from our previous approach, wherein the fluorescence is quenched *via* PET process to produce extra nonradiative heat and subsequently enhanced PA signals. The experimental and theoretical studies reveal that the higher heat interfacial conductance for the interface between the silica layer and water relative to that for the interface between the SP core and water leads to increased photothermal heating rate, consequently amplifying PA brightness for the silica-coated SPNs (SPNs-SiO_2) as compared to the uncoated SPNs. The proof-of-concept application of the amplified SPN (SPN1-SiO_2) is demonstrated for targeted PA imaging of tumor in living mice. With conjugation of PEG and cyclic-RGD to the surface of SPN1-SiO_2, it allows for more effective targeting to the 4T1 tumors of living mice as compared to the non-targeted nanoparticles after systemic administration. Our study thus not only provides a surface engineering approach to amplify the fluorescence and PA brightness for polymer nanoparticles but also reveals the important of increasing interfacial heat conductance in amplified PA imaging.

4. Experimental section

4.1. Chemicals

All chemicals were obtained from Sigma-Aldrich unless otherwise stated. 3-(4,5-Dimethylthiazol-2-yl)-5-(3-carboxymethoxyphenyl)-2-(4-sulfophenyl)-2H-tetrazolium, inner salt (MTS) solution were purchased from Promega, USA. Poly(cyclopentadithiophene-*alt*-benzothiadiazole) (PCPDTBT, SP2) was purchased from Luminescence Technology Corp.

Poly(cyclopentadithiophene-*alt*-diketopyrrolopyrrole) (PDPPCPDT, SP1) was synthesized in accordance with our previously published synthetic method [60]. *Cyclo* (RGDyC) was purchased from GL Biochem (Shanghai) Ltd. mPEG-NHS (MW: 2000) was purchased from Nanocs, USA.

4.2. Instrumentation

TEM images were obtained on a JEM 1400 transmission electron microscope with an accelerating voltage of 100 kv. Dynamic light scattering (DLS) was performed on the Malvern Nano-ZS Particle Size. Ultraviolet-visible (UV-Vis) spectra were obtained using a SHIMADZU UV-2450 spectrophotometer. Fluorescence measurements were carried out on a Fluorolog 3-TCSPC spectrofluorometer (Horiba JobinYvon). Infrared (IR) thermal images were recorded by the photothermal camera FLIR T420. An 808 nm high power NIR Lasers (operating mode: CW, output power after fiber: 2.5 W, LED display: diode current, multimode fiber, fiber core diameter: 400 μm, fiber connector: SMA905, with tunable laser driver module: 0-100%) purchased from CNI Co., Ltd. was used for photothermal measurements of SPNs solutions. The laser spot size was 1 cm^2. Fluorescence images of SPNs solutions were acquired with the IVIS spectrum imaging. Fluorescence images of SPN1 and SPN1-SiO_2 were acquired with excitation of 745 ± 10 nm, and emission at 820 ± 10 nm. Fluorescence images of SPN2 and SPN2-SiO_2 were acquired with excitation of 675 ± 10 nm, and emission at 820 ± 10 nm.

4.3. PA Instrumentation

For *in vitro* measurement, an optical parametric oscillator, OPO (Continuum, Surelite), which pumped by a Q-switched 532 nm Nd:YAG laser was used as an excitation source. OPO can generate tunable laser pulses within 680-900 nm wavelength range with 5 ns pulse duration, 100 mJ/pulse energy at 10 Hz repetition rate. The solution containing samples were placed inside a low-density polyethylene (LDPE) tube with an inner diameter (ID) of 0.59 mm and outer diameter (OD) of 0.78 mm. The sample containing LDPE tube, and the single-element ultrasound transducer, UST (V323-SU / 2.25 MHz, 13 mm active area, and 70% nominal bandwidth, Panametrics) were immersed into water medium for coupling of PA signals to UST. The LDPE tube was irradiated with wavelengths ranging from 680 - 900 nm with 10 nm increment. PA signals were collected using the UST and these signals were subsequently amplified using a gain of 50 dB, and band pass filtered (1-10 MHz) by a pulser/receiver unit (Olympus-NDT, 5072PR). Finally, the output signals from the pulser/receiver unit was digitized with a data acquisition card (GaGe, compuscope 4227) operated at 25 MHz and the acquired signals were stored in the computer. Peak-to-peak voltage of the PA signals was then normalized with the laser energy at each wavelength and were plotted against the wavelength to generate the PA spectrum. The PA signals at specific wavelength were measured using the same way. For *in vivo* measurement, a commercial Endra Nexus128 PA tomography system (Endra, Inc., Ann Arbor, MI) was used in this study. The system houses a tunable nanosecond pulsed laser (7 ns pulses, 20 Hz pulse repetition frequency, 9 mJ/pulse on the animal surface, wavelength range (680-950 nm)), 128 unfocused ultrasound transducers (with 5 MHz center frequency and 3 mm diameter) arranged in a hemispherical bowl filled with water, animal tray on top of the bowl, data acquisition/reconstruction console, servo motors for 3D rotation of the bowl, and a temperature monitor of the water bath.

4.4. Preparation of SPNs

SP (1 mg) was dissolved in THF (1 mL) by bath sonication. The resulted solutions were filtered through a polyvinylidene fluoride (PVDF) syringe driven filter (0.22 μm) (Millipore). SPNs-F were prepared *via* nanoprecipitation method. Briefly, a THF solution (1 mL) containing SP (0.25 mg) and F127 (25 mg) was used to prepare SPNs-F by rapidly injecting the solution into distilleddeionized water (9 mL) under continuous sonication with a bath sonicator Branson 250. After sonication for additional 120 s, THF was evaporated at room temperature with a gentle nitrogen flow. The aqueous solution was filtered through a polyethersulfone (PES) syringe driven filter (0.22 μm) (Millipore) to remove large nanoparticles. The obtained nanoparticle solutions were stored in dark at 4 ℃. SPN-S were synthesized as follow: Briefly, SP (0.5 mg) and F127 (50 mg) were dissolved in THF (1 mL) in a glass vial (10 mL) and stirred for 3 h at room temperature to obtain a homogeneous solution. After evaporating the THF solvent with a gentle nitrogen flow, a solid film was obtained and then redispersed in hydrochloride solution (0.85 M, 1.6 mL) with untrasonication to form a homogeneous suspension. Then the silica condensation was barked on by adding tetraethyl orthosilicate (TEOS) (90 μL) and subsequently stirring for 2 h at room temperature before adding (3-aminopropyl)triethoxysilane (APTS) (50 μL). The termination should last 24 h at room temperature with stirring. To remove hydrochloride and ethanol (resulted from the hydrolysis of TEOS and APTS), the product was washed and centrifuged four times at 3500 rpm for 30 min using an ultracentrifuge tube of 50 KDa (Millipore). The aqueous solution was filtered through a polyethersulfone (PES) syringe driven filter (0.22 μm) (Millipore). The obtained nanoparticle solutions were stored in dark at 4 ℃.

4.5. Synthesis of SPN1-SiO$_2$-PEG and SPN1-SiO$_2$-RGD

SPN1-S (1 mL, 20 μg mL^{-1}) was combined with 10 × PBS (110 μL, pH = 7.4), followed by the addition of mPEG-NHS (10 μL, 10 mg mL^{-1}). The mixture was stirred at room temperature for 2 h. The resulted SPN1-S-PEG were purified by three times washing using an ultracentrifuge tube of 50 KDa (Millipore) under centrifugation at 3500 rpm for 15 min. After the SPN1-S-PEG nanoparticles were obtained, EDC (60 μL, 5 mg mL^{-1}) and *Cyclo* (RGDyC) (40 μL, 1 mg mL^{-1}) were then added into the solution. The mixture was then stirred at room temperature overnight.

The resulted SPN1-S-RGD were purified by three times washing using an ultracentrifuge tube of 50 KDa (Millipore) under centrifugation at 3500 rpm for 15 min.

4.6. In Vitro Photothermal studies of SPNs

The 1×PBS buffer (pH 7.4) of SPNs (0.2 mL, 20 μg mL^{-1}) were exposed to laser of 808 nm (1 W cm^{-2}). The temperature was monitored using a photothermal camera (FLIR T420) every 20 s until reaching maxima after approximately 6 min. After the laser exposure, the temperature was continuously monitored every 20 s for 6 min. The heating and cooling were repeated five times to test the photothermal stability of SPNs.

4.7. Cell Culture and Cytotoxicity Test

4T1 human breast cancer epithelial cells were purchased from the American Type Culture Collection (ATCC). 4T1 cells were cultured in DMEM (Dulbecco's Modified Eagle Medium) (GIBCO) with 10% FBS (fetal bovine serum) (GIBCO) in a humidified environment containing 5% CO_2 and 95% air at 37 ℃. Cells were then seeded in 96 well plates (5000 cells in 200 μL per well) and cultured for 24 h, then SPN1-SiO_2-RGD or SPN1-SiO_2-PEG (final concentration 10, 25, 50 and 100 μg mL^{-1}) solutions were added into the cell culture medium separately. Cells were incubated for 24 h and followed by adding MTS (100 μL, 0.1 mg mL^{-1}) for another 4 h. The absorbance of MTS was measured by using a microplate reader at 490 nm. Cell viabilities were calculated by the ratio of the absorbance of the cells incubated with then SPN1-SiO_2-RGD or SPN1-SiO_2-PEG solution to that of the cells incubated with cell culture medium only.

4.8. Finite Element Simulation of PA Signals

The finite element analysis (FEA) simulation was conducted in COMSOL multiphysics (COMSOL Inc, USA.). For both photothermal and PA simulation, the laser irradiation on a single nanoparticle is assumed to be uniform, thus the temperature over the entire nanoparticle is also uniform and could be treated as heating source. For both nanoparticles in the simulation, the core has a semidiameter of 6 nm and specifically for SPN-SiO_2, a silica coating layer of thickness of 1 nm was added. The surrounding environment is set to be water. For photothermal effect simulation, the heat transfer module was used and the laser heating is continuous with the simulation run time to be 20 ns. For PA simulations, the laser heating pulse is set to 1 ns and the simulation were performed in two steps: in the first step, the heat transfer simulation was conducted using the heat transfer module in COMSOL; in the second step, the heat transfer simulation results were coupled to the acoustic module to obtain the final PA signals.

4.9 Tumor Mouse Model.

All animal experiments were performed in compliance with the Guidelines established by the Institutional Animal Care and Use Committee (IACUC), SingHealth. To establish tumor models in six-week-old female nu/nu mice, two million 4T1 cells which suspended in 50 mL of 50% v/v mixture of Matrigel in supplemented DMEM (10% fetal bovine serum, 1% pen/strep (100 U mL^{-1} penicillin and 100 µg mL^{-1} streptomycin) were injected subcutaneously in the shoulders of the mouse. Tumors were grown until a single aspect was ~7 mm (approximately 10-15 days) before being used for *in vivo* imaging experiments.

4.10. In Vivo PA imaging of tumor

Nude mice were anesthetized using 2% isoflurane in oxygen. The mice were placed in the Endra Nexus128 PA imaging system, and were scanned to determine the endogenous signal of tumors at 760 nm before systemically administration with SPN1-S-RGD (150 µg mL^{-1}, 0.2 mL) (n = 3) or SPN1-S-PEG (150 µg mL^{-1}, 0.2 mL) (n = 3) through the tail vein using a microsyringe. Data was acquired by a continuous model took 12 s to obtain one data set. Three dimensional PA images were reconstructed off-line using data acquired from all 128 transducers at each view and a back-projection algorithm. The algorithm corrects for pulse-to-pulse variations in the laser intensity and small changes in the temperature that affect acoustic velocity in the water. The reconstructed raw data is analyzed using OSiriX software. For *ex vivo* PA imaging, mice were sacrificed by CO_2 asphyxiation, organs were harvested and acquired immediately with Endra Nexus128 PA imaging system.

4.11. Data analysis

PA signal intensities were measured by region of interest (ROI) analysis using OsiriX. Results were expressed as the mean ± SD deviation unless otherwise stated. All statistical calculations were performed using GraphPad Prism v. 6 (GraphPad Software Inc., CA, USA).

Supporting Information

Supplementary data related to this article can be found at

Corresponding Author

*Email: kypu@ntu.edu.sg.

Notes

The authors declare no competing financial interest.

Acknowledgments

This work was supported by Nanyang Technological University start-up grant (NTU-SUG: M4081627.120), Academic Research Fund Tier 1 from Singapore Ministry of Education (RG133/15: M4011559) and Academic Research Fund Tier 2 from Ministry of Education in Singapore (MOE2016-T2-1-098).

References

[1] L.V. Wang, S. Hu, Photoacoustic tomography: *In vivo* imaging from organelles to organs, Science 335 (2012) 1458-1462.

[2] J. Weber, P.C. Beard, S.E. Bohndiek, Contrast agents for molecular photoacoustic imaging, Nat. Methods 13 (2016) 639-650.

[3] K.A. Homan, M. Souza, R. Truby, G.P. Luke, C. Green, E. Vreeland, S. Emelianov, Silver nanoplate contrast agents for *in vivo* molecular photoacoustic imaging, ACS Nano 6 (2012) 641-650.

[4] J. Zhang, X. Zhen, P.K. Upputuri, M. Pramanik, P. Chen, K. Pu, Activatable Photoacoustic Nanoprobes for *in vivo* Ratiometric Imaging of Peroxynitrite, Adv. Mater. (2016) DOI: 10.1002/adma.201604764.

[5] X. Wang, Y. Pang, G. Ku, X. Xie, G. Stoica, L.V. Wang, Noninvasive laser-induced photoacoustic tomography for structural and functional *in vivo* imaging of the brain, Nature Biotechnol. 21 (2003) 803-806.

[6] D. Pan, M. Pramanik, A. Senpan, J.S. Allen, H. Zhang, S.A. Wickline, L.V. Wang, G.M. Lanza, Molecular photoacoustic imaging of angiogenesis with integrin-targeted gold nanobeacons, The FASEB J 25 (2011) 875-882.

[7] J.V. Jokerst, A.J. Cole, D. Van de Sompel, S.S. Gambhir, Gold nanorods for ovarian cancer detection with photoacoustic imaging and resection guidance *via* Raman imaging in living mice, ACS Nano 6 (2012) 10366-10377.

[8] J. Laufer, P. Johnson, E. Zhang, B. Treeby, B. Cox, B. Pedley, P. Beard, *In Vivo* preclinical photoacoustic imaging of tumor vasculature development and therapy, J. Biomed. Opt. 17 (2012) 0560161-0560168.

[9] W.J. Akers, C. Kim, M. Berezin, K. Guo, R. Fuhrhop, G.M. Lanza, G.M. Fischer, E. Daltrozzo, A. Zumbusch, X. Cai, L.V. Wang, S. Achilefu, Noninvasive photoacoustic and fluorescence sentinel lymph node identification using dye-loaded perfluorocarbon nanoparticles, ACS Nano 5 (2010) 173-182.

[10] M.F. Kircher, A. De La Zerda, J.V. Jokerst, C.L. Zavaleta, P.J. Kempen, E. Mittra, K. Pitter, R. Huang, C. Campos, F. Habte, R. Sinclair, C.W. Brennan, I.K. Mellinghoff, E.C. Holland, S.S.

Gambhir, A brain tumor molecular imaging strategy using a new triple-modality MRI-photoacoustic-Raman nanoparticle, Nat. Med. 18 (2012) 829-834.

[11] H.J. Lee, Y. Liu, J. Zhao, M. Zhou, R.R. Bouchard, T. Mitcham, M. Wallace, R.J. Stafford, C. Li, S. Gupta, M.P. Melancon, *In vitro* and *in vivo* mapping of drug release after laser ablation thermal therapy with doxorubicin-loaded hollow gold nanoshells using fluorescence and photoacoustic imaging, J. Control. Release 172 (2013) 152-158.

[12] B. Wang, Q. Zhao, N.M. Barkey, D.L. Morse, H. Jiang, Photoacoustic tomography and fluorescence molecular tomography: A comparative study based on indocyanine green, Med. Phys. 39 (2012) 2512-2517.

[13] Q. Fan, K. Cheng, Z. Yang, R. Zhang, M. Yang, X. Hu, X. Ma, L. Bu, X. Lu, X. Xiong, W. Huang, H. Zhao, Z. Cheng, Perylene-Diimide-Based nanoparticles as highly efficient photoacoustic agents for deep brain tumor imaging in living mice, Adv. Mater. 27 (2015) 843-847.

[14] J. Wang, F. Chen, S.J. Arconada-Alvarez, J. Hartanto, L.-P. Yap, R. Park, F. Wang, I. Vorobyova, G. Dagliyan, P.S. Conti, J.V. Jokerst, A nanoscale tool for photoacoustic-based measurements of clotting time and therapeutic drug monitoring of heparin, Nano Lett. 16 (2016) 6265-6271.

[15] R.M. Hoffman, The multiple uses of fluorescent proteins to visualize cancer *in vivo*, Nat. Rev. Cancer 5 (2005) 796-806.

[16] G.S. Filonov, A. Krumholz, J. Xia, J. Yao, L.V. Wang, V.V. Verkhusha, Deep-tissue photoacoustic tomography of a genetically encoded near-infrared fluorescent probe, Angew. Chem. Int. Ed. 51 (2012) 1448-1451.

[17] M. Chen, S. Tang, Z. Guo, X. Wang, S. Mo, X. Huang, G. Liu, N. Zheng, Core–shell Pd@ Au nanoplates as theranostic agents for *in-vivo* photoacoustic imaging, CT imaging, and photothermal therapy, Adv. Mater. 26 (2014) 8210-8216.

[18] A. De La Zerda, C. Zavaleta, S. Keren, S. Vaithilingam, S. Bodapati, Z. Liu, J. Levi, B.R. Smith, T.-J. Ma, O. Oralkan, Z. Cheng, X. Chen, H. Dai, B.T. Khuri-Yakub, S.S. Gambhir, Carbon nanotubes as photoacoustic molecular imaging agents in living mice, Nat. Nanotechnol. 3 (2008) 557-562.

[19] C. Wang, X. Ma, S. Ye, L. Cheng, K. Yang, L. Guo, C. Li, Y. Li, Z. Liu, Protamine functionalized single-walled carbon nanotubes for stem cell labeling and in vivo raman/magnetic resonance/photoacoustic triple-modal imaging, Adv. Funct. Mater. 22 (2012) 2363-2375.

[20] A. De La Zerda, Z. Liu, S. Bodapati, R. Teed, S. Vaithilingam, B.T. Khuri-Yakub, X. Chen, H. Dai, S.S. Gambhir, Ultrahigh sensitivity carbon nanotube agents for photoacoustic molecular imaging in living mice, Nano Lett. 10 (2010) 2168-2172.

[21] J.-W. Kim, E.I. Galanzha, E.V. Shashkov, H.-M. Moon, V.P. Zharov, Golden carbon nanotubes as multimodal photoacoustic and photothermal high-contrast molecular agents, Nat. Nanotechnol. 4 (2009) 688-694.

[22] K. Yang, L. Hu, X. Ma, S. Ye, L. Cheng, X. Shi, C. Li, Y. Li, Z. Liu, Multimodal imaging guided photothermal therapy using functionalized graphene nanosheets anchored with magnetic nanoparticles, Adv. Mater. 24 (2012) 1868-1872.

[23] Z. Sheng, L. Song, J. Zheng, D. Hu, M. He, M. Zheng, G. Gao, P. Gong, P. Zhang, Y. Ma, L. Cai, Protein-assisted fabrication of nano-reduced graphene oxide for combined *in vivo* photoacoustic imaging and photothermal therapy, Biomaterials 34 (2013) 5236-5243.

[24] M.A. Patel, H. Yang, P.L. Chiu, D.D. Mastrogiovanni, C.R. Flach, K. Savaram, L. Gomez, A. Hemnarine, R. Mendelsohn, E. Garfunkel, H. Jiang, H. He, Direct production of graphene nanosheets for near infrared photoacoustic imaging, ACS Nano 7 (2013) 8147-8157.

[25] X. Ai, C.J.H. Ho, J. Aw, A.B.E. Attia, J. Mu, Y. Wang, X. Wang, Y. Wang, X. Liu, H. Chen, M. Gao, X. Chen, E.K.L. Yeow, G. Liu, M. Olivo, B. Xing, *In vivo* covalent cross-linking of photon-converted rare-earth nanostructures for tumour localization and theranostics, Nat. Commun. 7 (2016) 10432.

[26] J.F. Lovell, C.S. Jin, E. Huynh, H. Jin, C. Kim, J.L. Rubinstein, W.C. Chan, W. Cao, L.V. Wang, G. Zheng, Porphysome nanovesicles generated by porphyrin bilayers for use as multimodal biophotonic contrast agents, Nat. Mater. 10 (2011) 324-332.

[27] E. Huynh, C.S. Jin, B.C. Wilson, G. Zheng, Aggregate enhanced trimodal porphyrin shell microbubbles for ultrasound, photoacoustic, and fluorescence imaging, Bioconjugate Chem. 25 (2014) 796-801.

[28] E. Huynh, J.F. Lovell, B.L. Helfield, M. Jeon, C. Kim, D.E. Goertz, B.C. Wilson, G. Zheng, Porphyrin shell microbubbles with intrinsic ultrasound and photoacoustic properties, J. Am. Chem. Soc. 134 (2012) 16464-16467.

[29] J. Yu, Y. Rong, C.-T. Kuo, X.-H. Zhou, D.T. Chiu, Recent advances in the development of highly luminescent semiconducting polymer dots and nanoparticles for biological imaging and medicine, Anal. Chem. 89 (2016) 42-56.

[30] C. Wu, D.T. Chiu, Highly fluorescent semiconducting polymer dots for biology and medicine, Angew. Chem. Int. Ed. 52 (2013) 3086-3109.

[31] L. Feng, C. Zhu, H. Yuan, L. Liu, F. Lv, S. Wang, Conjugated polymer nanoparticles: preparation, properties, functionalization and biological applications, Chem. Soc. Rev. 42 (2013) 6620-6633.

[32] K. Pu, N. Chattopadhyay, J. Rao, Recent advances of semiconducting polymer nanoparticles in *in vivo* molecular imaging, J. Control. Release 240 (2016) 312-322.

[33] X. Zhen, C. Zhang, C. Xie, Q. Miao, K.L. Lim, K. Pu, Intraparticle energy level alignment of semiconducting polymer nanoparticles to amplify chemiluminescence for ultrasensitive *in vivo* imaging of reactive oxygen species, ACS Nano 10 (2016) 6400-6409.

[34] A.J. Shuhendler, K. Pu, L. Cui, J.P. Uetrecht, J. Rao, Real-time imaging of oxidative and nitrosative stress in the liver of live animals for drug-toxicity testing, Nat. Biotechnol. 32 (2014) 373-380.

[35] C. Xie, P.K. Upputuri, X. Zhen, M. Pramanik, K. Pu, Self-quenched semiconducting polymer nanoparticles for amplified in vivo photoacoustic imaging, Biomaterials 119 (2017) 1-8.

[36] C. Xie, X. Zhen, Q. Lei, R. Ni, K. Pu, Self-assembly of semiconducting polymer amphiphiles for *in vivo* photoacoustic imaging, Adv. Funct. Mater. (2017) DOI: 10.1002/adfm.201605397.

[37] H.-Y. Liu, P.-J. Wu, S.-Y. Kuo, C.-P. Chen, E.-H. Chang, C.-Y. Wu, Y.-H. Chan, Quinoxaline-based polymer dots with ultrabright red to near-infrared fluorescence for *in vivo* biological imaging, J. Am. Chem. Soc. 137 (2015) 10420-10429.

[38] K. Sun, Y. Tang, Q. Li, S. Yin, W. Qin, J. Yu, D.T. Chiu, Y. Liu, Z. Yuan, X. Zhang, C. Wu *In vivo* dynamic monitoring of small molecules with implantable polymer-dot transducer, ACS Nano 10 (2016) 6769-6781.

[39] Q. Miao, K. Pu, Emerging Designs of activatable photoacoustic probes for molecular imaging, Bioconjugate Chem. 27 (2016) 2808-2823.

[40] Y. Lyu, X. Zhen, Y. Miao, K. Pu, Reactivity-based semiconducting polymer nanoprobes for photoacoustic imaging of protein sulfenic acids, ACS Nano (2017) DOI: 10.1021/acsnano.6b05949.

[41] K. Pu, A.J. Shuhendler, J.V. Jokerst, J. Mei, S.S. Gambhir, Z. Bao, J. Rao, Semiconducting polymer nanoparticles as photoacoustic molecular imaging probes in living mice, Nat. Nanotechnol. 9 (2014) 233-239.

[42] Q. Miao, Y. Lyu, D. Ding, K. Pu, Semiconducting oligomer nanoparticles as an activatable photoacoustic probe with amplified brightness for *in vivo* imaging of pH, Adv. Mater. 28 (2016) 3662-3668.

[43] K. Pu, A.J. Shuhendler, J. Rao, Semiconducting polymer nanoprobe for in vivo imaging of reactive oxygen and nitrogen species, Angew. Chem. Int. Ed. 52 (2013) 10325-10329.

[44] K. Pu, J. Mei, J.V. Jokerst, G. Hong, A.L. Antaris, N. Chattopadhyay, A.J. Shuhendler, T. Kurosawa, Y. Zhou, S.S. Gambhir, Z. Bao, J. Rao, Diketopyrrolopyrrole-based semiconducting polymer nanoparticles for *in vivo* photoacoustic imaging, Adv. Mater. 27 (2015) 5184-5190.

[45] Y. Lyu, Y. Fang, Q. Miao, X. Zhen, D. Ding, K. Pu, Intraparticle molecular orbital engineering of semiconducting polymer nanoparticles as amplified theranostics for *in vivo* photoacoustic imaging and photothermal therapy, ACS Nano 10 (2016) 4472-4481.

[46] J. Chen, C. Liu, D. Hu, F. Wang, H. Wu, X. Gong, X. Liu, L. Song, Z. Sheng, H. Zheng, Single‐Layer MoS2 Nanosheets with Amplified Photoacoustic Effect for Highly Sensitive Photoacoustic Imaging of Orthotopic Brain Tumors, Adv. Funct. Mater. 26 (2016) 8715-8725.

[47] H. Moon, D. Kumar, H. Kim, C. Sim, J.-H. Chang, J.-M. Kim, H. Kim, D.-K. Lim, Amplified photoacoustic performance and enhanced photothermal stability of reduced graphene oxide coated gold nanorods for sensitive photoacoustic imaging, ACS Nano 9 (2015) 2711-2719.

[48] Y. Chen, H. Chen, J. Shi, *In vivo* bio-safety evaluations and diagnostic/therapeutic applications of chemically designed mesoporous silica nanoparticles, Adv. Mater. 25 (2013) 3144-3176.

[49] Z. Ge, Y. Kang, T.A. Taton, P.V. Braun, D.G. Cahill, Thermal transport in Au-core polymer-shell nanoparticles, Nano Lett. 5 (2005) 531-535.

[50] A. Plech, V. Kotaidis, S. Grésillon, C. Dahmen, G. Von Plessen, Laser-induced heating and melting of gold nanoparticles studied by time-resolved X-ray scattering, Phys. Rev. B 70 (2004) 195423.

[51] Y.-S. Chen, W. Frey, S. Kim, P. Kruizinga, K. Homan, S. Emelianov, Silica-coated gold nanorods as photoacoustic signal nanoamplifiers, Nano Lett. 11 (2011) 348-354.

[52] H. Zhu, Y. Fang, X. Zhen, N. Wei, Y. Gao, K.Q. Luo, C. Xu, H. Duan, D. Ding, P. Chen, K. Pu, Multilayered semiconducting polymer nanoparticles with enhanced NIR fluorescence for molecular imaging in cells, zebrafish and mice, Chem. Sci. 7 (2016) 5118-5125.

[53] J.E. Lee, N. Lee, H. Kim, J. Kim, S.H. Choi, J.H. Kim, T. Kim, I.C. Song, S.P. Park, W.K. Moon, T. Hyeon, Uniform mesoporous dye-doped silica nanoparticles decorated with multiple magnetite nanocrystals for simultaneous enhanced magnetic resonance imaging, fluorescence imaging, and drug delivery, J. Am. Chem. Soc. 132 (2009) 552-557.

[54] Q. Huo, J. Liu, L.-Q. Wang, Y. Jiang, T.N. Lambert, E. Fang, A new class of silica cross-linked micellar core-shell nanoparticles, J. Am. Chem. Soc. 128 (2006) 6447-6453.

[55] S. Murad, I.K. Puri, Molecular simulation of thermal transport across hydrophilic interfaces, Chem. Phys. Lett. 467 (2008) 110-113.

[56] D.G. Cahill, W.K. Ford, K.E. Goodson, G.D. Mahan, A. Majumdar, H.J. Maris, R. Merlin, S.R. Phillpot, Nanoscale thermal transport, J. Appl. Phys. 93 (2003) 793-818.

[57] M. Xu, L.V. Wang, Photoacoustic imaging in biomedicine, Rev. Sci. Instrum. 77 (2006) 041101.

[58] M.A. Dechantsreiter, E. Planker, B. Mathä, E. Lohof, G. Hölzemann, A. Jonczyk, S.L. Goodman, H. Kessler, N-Methylated cyclic RGD peptides as highly active and selective αvβ3 integrin antagonists, J. Med. Chem. 42 (1999) 3033-3040.

[59] J.K. Willmann, A.M. Lutz, R. Paulmurugan, M.R. Patel, P. Chu, J. Rosenberg, S.S. Gambhir, Dual-targeted contrast agent for US assessment of tumor angiogenesis *in vivo,* Radiology 248 (2008) 936-944.

[60] Y. Lyu, C. Xie, S.A. Chechetka, E. Miyako, K. Pu, Semiconducting polymer nanobioconjugates for targeted photothermal activation of neurons, J. Am. Chem. Soc. 138 (2016) 9049-9052.

Table of Contents Graphic